The Astrophysical Journal, 902:20 (12pp), 2020 October 10 https://doi.org/10.3847/1538-4357/abb2a4

Small Electron Events Observed by Parker Solar Probe/IS⊙IS during Encounter 2

J. G. Mitchell[1,2], G. A. de Nolfo[2], M. E. Hill[3], E. R. Christian[2], D. J. McComas[4], N. A. Schwadron[5], M. E. Wiedenbeck[6], S. D. Bale[7,8,9,10], A. W. Case[11], C. M. S. Cohen[12], C. J. Joyce[4], J. C. Kasper[11,13], A. W. Labrador[12], R. A. Leske[12], R. J. MacDowall[14], R. A. Mewaldt[12], D. G. Mitchell[3], M. Pulupa[8], I. G. Richardson[2,15], M. L. Stevens[11], and J. R. Szalay[4]
[1] Department of Physics, George Washington University, Washington, DC 20052, USA; john.g.mitchell@nasa.gov
[2] NASA Goddard Space Flight Center, Greenbelt, MD 20771, USA
[3] Johns Hopkins University, Applied Physics Laboratory, Laurel, MD 20723, USA
[4] Department of Astrophysical Sciences, Princeton University, Princeton, NJ 08544, USA
[5] University of New Hampshire, Durham, NH 03824, USA
[6] Jet Propulsion Laboratory, California Institute of Technology, Pasadena, CA 91109, USA
[7] Physics Department, University of California, Berkeley, CA 94720-7300, USA
[8] Space Sciences Laboratory, University of California, Berkeley, CA 94720-7450, USA
[9] The Blackett Laboratory, Imperial College London, London SW7 2AZ, UK
[10] School of Physics and Astronomy, Queen Mary University of London, London E1 4NS, UK
[11] Smithsonian Astrophysical Observatory, Cambridge, MA 02138, USA
[12] California Institute of Technology, Pasadena, CA 91125, USA
[13] Climate and Space Sciences and Engineering, University of Michigan, Ann Arbor, MI 48109, USA
[14] Solar System Exploration Division, NASA/Goddard Space Flight Center, Greenbelt, MD 20771, USA
[15] GPHI and Department of Astronomy, University of Maryland, College Park, MD 20742, USA
Received 2020 May 20; revised 2020 July 24; accepted 2020 August 24; published 2020 October 8

Abstract

The current understanding of the characteristics of solar and inner heliospheric electron events is inferred almost entirely from observations made by spacecraft located at 1 astronomical unit (au). Previous observations within 1 au of the Sun, by the Helios spacecraft at ∼0.3–1 au, indicate the presence of electron events that are not detected at 1 au or may have merged during transport from the Sun. Parker Solar Probe's close proximity to the Sun at perihelion provides an opportunity to make the closest measurements yet of energetic electron events. We present an overview of measurements of electrons with energies between ∼17 keV and ∼1 MeV made by the Parker Solar Probe Integrated Science Investigation of the Sun (IS⊙IS) instrument suite during Encounter 2 (2019 March 31–April 10 with perihelion of ∼0.17 au), including several small electron events. We examine these events in the context of the electromagnetic and solar wind environment measured by the FIELDS and SWEAP instruments on Parker Solar Probe. We find most of these electron enhancements to be associated with type III radio emissions that reach the local plasma frequency and one enhancement that appears to be primarily associated with abrupt changes in the local magnetic field. Together, these associations suggest that these are indeed the first measurements of energetic electron events within 0.2 au.

Unified Astronomy Thesaurus concepts: Solar flares (1496); Solar energetic particles (1491); Solar particle emission (1517); Radio bursts (1339); Solar physics (1476)

1. Introduction

Energetic electron enhancements have been observed in situ since the earliest observations in the 1960s (e.g., Arnoldy et al. 1960; Hoffman et al. 1962; Frank 1965; Van Allen & Krimigis 1965; Anderson & Lin 1966) made with spacecraft such as Pioneer 5, Explorer 12, Explorer 14, Mariner 4, IMP-1, and IMP-3. A variety of acceleration sources at the Sun or within the local interplanetary medium produce electron enhancements, including solar jets and flares, coronal mass ejections (CMEs), and magnetic reconnection in the solar wind. Parker Solar Probe allows us to probe these diverse sources of electrons at previously unreached heliocentric distances, providing an opportunity to examine very small electron events that may not be observable at 1 au.

The study of solar energetic particle (SEP) events shows that these events are frequently observed to have significant enhancements in energetic electrons (Lin 1970, 1985). Many electron-rich solar particle events are accompanied by ^{3}He (Hsieh & Simpson 1970; Wang et al. 2012), heavy ions (Hurford et al. 1975), and even ultraheavy (trans-iron) ions (Reames & Ng 2004). For example, Wang et al. (2012) found a 76% association between ^{3}He-rich emissions and solar electron events. These characteristics, among others including duration and association with type III radio bursts, are used to identify traditional "impulsive" SEP events (Reames 2013). It is widely believed that magnetic reconnection between open and closed field lines (Crooker et al. 2002; Reames 2002; Crooker & Webb 2006) drives impulsive SEP events. Current theories suggest that reconnection leads to the formation of islands. Particles are accelerated as they interact with contracting islands, with the larger islands accelerating the heavier ions with larger gyroradii (e.g., Drake et al. 2006, 2009; Drake & Swisdak 2012). These accelerated charged particles may then escape the solar corona along open field lines (Krucker et al. 2011). Lower energy electrons (<25 keV) travel largely scatter-free through the interplanetary medium, while higher energy electrons experience pitch-angle scattering and diffusive transport (Dröge 2000; Tan et al. 2011; Wang et al. 2011).

A key signature of electrons escaping the solar corona is the presence of type III radio bursts produced by streaming ~2–25 keV electrons (Lin 1974; Lin et al. 1981, 1986; Buttighoffer 1998; Ergun et al. 1998; Reid & Ratcliffe 2014). Streaming electrons may generate Langmuir waves, which induce electromagnetic emission at the electron plasma frequency, proportional to $\sqrt{n_e}$, where n_e is the electron density in the solar wind (Bastian et al. 1998). As the electrons propagate away from the Sun through the solar corona and interplanetary medium, the local n_e decreases, resulting in the characteristic fast drift of type III radio bursts from high frequencies to lower frequencies. Wang et al. (2012) found that 98.75% of solar electron events from ~0.1 to 310 keV are preceded by a type III radio burst. On the other hand, there are many more type III events than detected solar electron events, suggesting that streaming electron events are relatively common but may not reach the observing spacecraft, for example if weak or poorly connected to the spacecraft, and the type III emission then does not reach the plasma frequency at the observer's location (Dulk et al. 1998; Cane & Erickson 2003).

Higher-energy solar electrons (>10–15 keV) are frequently observed to be delayed with respect to the lower energy electrons responsible for the type III radio emission (Krucker et al. 1999; Haggerty & Roelof 2002; Klassen et al. 2002; Cane 2003; Wang et al. 2006, 2016). Krucker et al. (1999), Klassen et al. (2002), Haggerty & Roelof (2002), and Wang et al. (2006, 2016) argue that the near-relativistic electrons observed in situ are a separate population, injected later than the lower energy electrons that produce the radio burst, whereas Cane (2003) suggests that both are part of the same population. Cane (2003) suggests that the higher energy electrons are delayed in transit through the interplanetary medium, though Wang et al. (2011) demonstrated that the increased path length due to scattering of high-energy electrons appears too short to explain the observed delays in the high-energy electrons. Observations of energetic electrons by Parker Solar Probe may help to shed new light on these types of questions due to the reduction of transport effects close to the Sun.

Previous observations by the Helios spacecraft, reported by Wibberenz & Cane (2006), demonstrate that electron events are present in the inner heliosphere that are not detected at 1 au, presumably because they did not reach the observing spacecraft or were too weak to be observed due to instrumental backgrounds or sensitivity (e.g., Wang et al. 2012). Events may also have merged before reaching 1 au, likely due to transport effects in the interplanetary medium.

We present the first measurements of energetic electrons within 0.2 au, made around Parker Solar Probe's second perihelion pass on 2019 April 4 (DOY 94). These tiny events have peak intensities[16] of ~1 $cm^{-2}\,sr^{-1}\,s^{-1}\,MeV^{-1}$ for EPI-Hi (~0.5–1 MeV) and ~2×10^3 $cm^{-2}\,sr^{-1}\,s^{-1}\,MeV^{-1}$ for EPI-Lo (~17–400 keV) and durations of less than one hour. These intensities are much lower than previously reported for electron events. For example, Bieber et al. (1980) observed a peak intensity of nearly 10^6 $cm^{-2}\,sr^{-1}\,s^{-1}\,MeV^{-1}$ at ~0.5 MeV from Helios 2 measurements at 0.5 au in an event that lasted >24 hr. Bialk & Dröge (1993) observed peak electron fluxes of ~10 $cm^{-2}\,sr^{-1}\,s^{-1}\,MeV^{-1}$ at higher energies (~2 MeV) on Helios 1 at 0.95 au in an event lasting several hours. The Helios electron events reported by Wibberenz & Cane (2006) are only reported in arbitrary units, but they all have peak fluxes 1–3 orders of magnitude above background level and persisted for several hours. A number of small events have been observed and compiled by the STEREO/IMPACT/SEPT team (Dresing et al. 2020). Some of these events have very small enhancements above background; however, these events have longer durations, resulting in a higher event particle fluence than the events in the present study. Due to the low count rates of the events in the present study (defined as events with a composite signal-to-background ratio of 3.5–10, described in Section 3 and Appendix A), it is challenging to distinguish a true electron event from background. We take advantage of statistical techniques and contemporaneous radio, magnetic fields, and plasma data measured by instruments on board Parker Solar Probe to attempt to identify real electron events that stand out above the background and may be the result of solar or inner heliospheric acceleration processes.

2. Parker Solar Probe

Parker Solar Probe (Fox et al. 2016) was launched on 2018 August 12 into a heliocentric orbit. Over its planned 7 yr mission lifetime, Parker Solar Probe's perihelion distance will gradually decrease using Venus flybys and the probe will pass directly through the solar corona, within about nine solar radii above the surface of the Sun (with the first closest approach taking place on 2024 December 24). The broad science goals of Parker Solar Probe are to make measurements that further the understanding of how energy moves through the solar corona and to gain new insight into the processes that accelerate the solar wind and SEPs. To accomplish these goals, Parker Solar Probe carries four scientific instrument suites: Solar Wind Electrons, Alphas and Protons investigation (SWEAP), designed to investigate the solar wind plasma (Kasper et al. 2016); Electromagnetic Fields Investigation (FIELDS), which investigates the complex solar electromagnetic fields (Bale et al. 2016); Wide-field Imager for Solar Probe (WISPR), which investigates CMEs and other structures through white-light imagery (Vourlidas et al. 2016); and Integrated Science Investigation of the Sun (IS⊙IS), a suite of particle instruments that provides information on the characteristics of the energetic particle population (McComas et al. 2016).

2.1. The IS⊙IS Instrument Suite

The IS⊙IS Energetic Particle Instruments (EPI) measure the composition and energy spectra of low-energy (EPI-Lo) and high-energy (EPI-Hi) particles. EPI-Lo is a mass spectrometer that uses time-of-flight (TOF) within the instrument and energy deposited in a solid state detector (SSD) to determine the incident particle's energy and species together with its approximate arrival direction. EPI-Lo measures ions from ~20 keV/nucleon to 20 MeV/nucleon; in this study, we focus on electrons measured in the ~17 keV–400 keV range, utilizing only the SSD system, consisting of an SSD covered by a ~3.2 μm thick aluminum flashing in each instrumental wedge. EPI-Lo provides an approximately 2π sr field of view with good coverage in the sunward, antisunward, and nominal

[16] As it is early in the mission, the IS⊙IS electron intensities are not fully calibrated at the time of writing. These figures are approximated from the peak count rate, assuming a flat distribution and estimates of geometry factors of 0.056 cm^2 sr for EPI-Lo from Hill et al. (2017) and 0.5 cm^2 sr for both EPI-Hi HET and LET from Wiedenbeck et al. (2017).

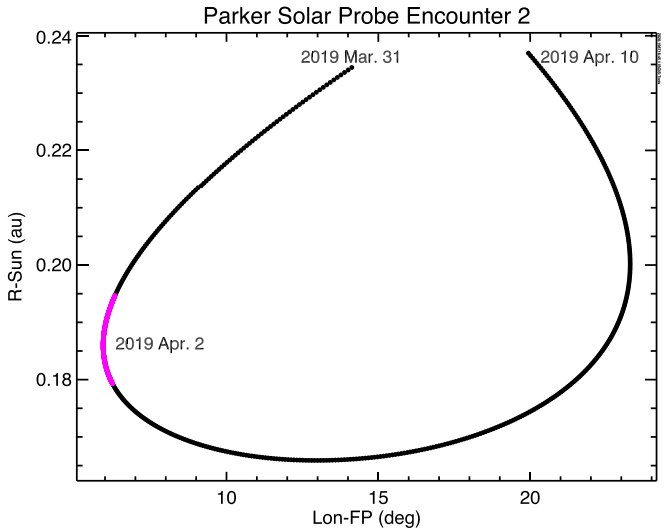

Figure 1. The solar radius of Parker Solar Probe vs. the Carrington longitude of the spacecraft's magnetic solar footpoint, assuming a nominal Parker spiral with a solar wind speed of 350 km s^{-1} through Encounter 2 (with 2019 April 2 highlighted in magenta). The narrow range of footpoint longitudes on this day shows that Parker Solar Probe is in co-rotation with the Sun.

Parker spiral directions, from eight wedges arranged in an octagonal configuration.

The EPI-Hi telescopes make measurements using a standard "dE/dx versus total E" technique. EPI-Hi is composed of layers of SSDs, such that the energy and species of a particle can be determined based on the total energy deposited in the detectors and the rate of particle energy loss as a function of detector thickness traversed. EPI-Hi comprises three telescopes: a high-energy, double-ended telescope (HET with apertures referred to as HET-A and HET-B) and two low-energy telescopes (LET1 and LET2). LET1 is double-ended (with apertures referred to as LET-A and LET-B) and LET2 is single-ended (with a single aperture referred to as LET-C). The axes of all five apertures lie in the plane of the spacecraft's orbit in its nominal orientation. The HET-A aperture is approximately aligned with the nominal Parker spiral direction when the spacecraft is located at 0.25 au. The LET-A aperture is approximately 25° offset from HET-A. HET-B and LET-B face directions opposite to HET-A and LET-A, respectively. LET-C is rotated 90° from LET-A, pointing approximately in the ram direction of the spacecraft (McComas et al. 2016; Wiedenbeck et al. 2017). Together, the EPI-Hi telescopes sample energetic particles with wide angular coverage. EPI-Hi measures 0.5–6 MeV electrons and 1–200 MeV/nucleon ions.

3. Overview of Encounter 2

Parker Solar Probe's orbits are divided into two separate segments based on the spacecraft's heliocentric distance. The "encounter" periods are defined as the time when Parker Solar Probe is within 0.25 au. The remainder of the orbit is defined as the "cruise" phase, during which the science instruments are not continuously operating and typically record data at a lower rate. Parker Solar Probe's second encounter took place during 2019 March 31–April 10 (DOY 90–100), with its second perihelion occurring on 2019 April 4 (DOY 94) and reaching a minimum solar distance of ∼0.17 au. Figure 1 shows Parker Solar Probe's solar radius versus the Carrington longitude of the spacecraft's magnetic solar footpoint, assuming a nominal Parker spiral with a solar wind speed of 350 km s^{-1} during the time period of Encounter 2. The day of particular interest in this study, 2019 April 2 (DOY 92), has been highlighted in magenta. During this day, Parker Solar Probe remained within half a degree of the same solar footpoint, demonstrating that the spacecraft was co-rotating with the Sun. Parker Solar Probe had a Heliocentric Earth Ecliptic (HEE) longitude (Thompson 2006) between −95° and −85° with respect to the Sun–Earth line on 2019 April 2 (DOY 92). McComas et al. (2019) examined the energetic particle observations over Orbits 1 and 2 and reported a variety of high- and low-energy events, extending down through previously unexplored regions of the inner heliosphere. The beginning of Parker Solar Probe's mission took place during solar minimum, in a period of very low solar activity. As a result, Parker Solar Probe did not observe any large, temporally extended solar energetic particle events during these orbits, which provided a novel opportunity to examine individual small electron events that may be harder to distinguish during future orbits when solar activity will be higher.

Context for the electron observations is provided by solar radio emissions detected by the V1–V4 electric field probes on the FIELDS instrument. Parker Solar Probe's first two encounters showed remarkably different radio emissions due to the emergence of an active region (NOAA AR 12738) shortly before the start of Encounter 2 (Pulupa et al. 2020). FIELDS only observed a small number of radio bursts during Parker Solar Probe's first encounter, in stark contrast with the hundreds of type III radio bursts and many groups of Langmuir waves observed during Parker Solar Probe's second encounter. The strong connection between type III radio bursts and impulsive electron events naturally leads to a careful examination of potential electron events and the concurrent radio observations. Context is also provided by data from the FIELDS magnetometers and from the Solar Probe Analyzers (SPAN) in the SWEAP instrument suite, designed to measure the velocity distribution functions of solar wind ions and electrons (Whittlesey et al. 2020). Of particular interest here, SPAN is capable of measuring electrons with energies of 2 eV–30 keV, but during Parker Solar Probe's first two encounters, the upper energy limit was set to 2 keV (Halekas et al. 2020). EPI-Lo is sensitive to >17 keV electrons, which is near the upper limit of the energy range (∼2–25 keV) of the electrons believed to be responsible for generating the Langmuir waves that give rise to type III radio emission. Although observations at these critical energies are not available, the energetic electron population may extend into the EPI-Lo energy range (e.g., Lin et al. 1997; Dulk et al. 1998; Cane 2003) so that the presence of the lower energy electrons may be inferred from the observations of electrons at slightly higher energies by EPI-Lo.

4. Observations of Electron Events during Encounter 2

Figure 2 shows an overview of the electron, magnetic field, radio, and solar wind data from Parker Solar Probe's second encounter. Panels (a) and (b) of Figure 2 show EPI-Hi and EPI-Lo electron count rate data over the course of Encounter 2. The EPI-Hi data are the sum of the electron count rates from the shortest electron ranges in EPI-Hi: HET apertures A and B range 1 and LET1 and 2 apertures A, B, and C range 3, where "range" is assigned based on the number of SSDs traversed (Wiedenbeck et al. 2017). The EPI-Lo data are summed over

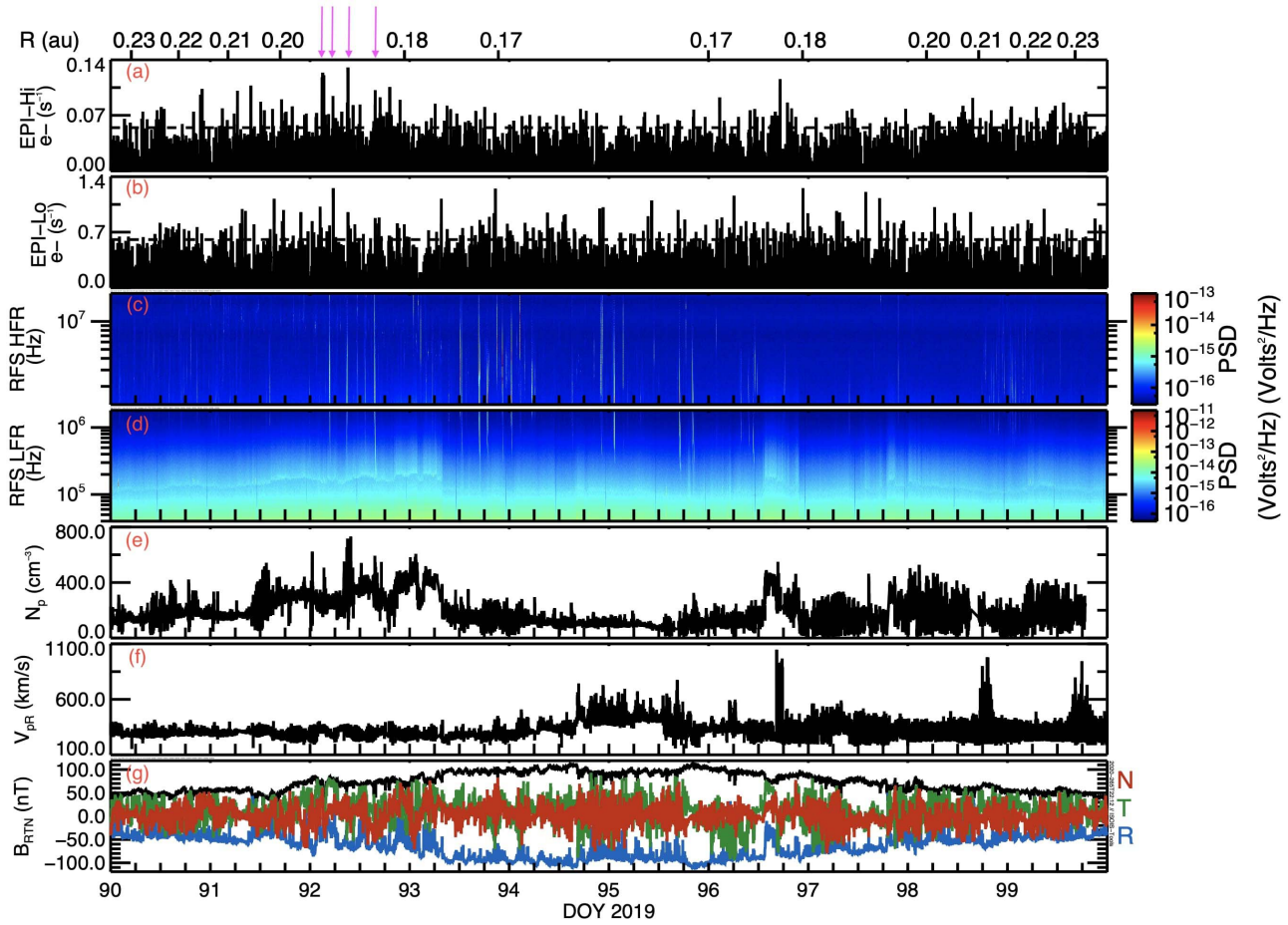

Figure 2. Overview of Parker Solar Probe Encounter 2. The top axis displays the spacecraft's solar radial distance in au. Arrows above the figure indicate the energetic electron events presented in this work. Panels from top to bottom are (a) background-subtracted and 7 minutes Savitzky–Golay smoothed EPI-Hi electron count rate (0.5–6 MeV) with a dashed line to indicate 2σ deviation from the mean, (b) background-subtracted and 7 minutes Savitzky–Golay smoothed EPI-Lo electron count rate (50–500 keV) with a dashed line to indicate 2σ deviation from the mean, (c) high-frequency radio measurements by FIELDS (1.3–19.2 MHz), (d) low-frequency radio measurements by FIELDS (10.5 kHz–1.7 MHz), (e) solar wind ion density moment measured by SWEAP (∼5 measurements per second), (f) radial component of solar wind velocity moment measured by SWEAP (∼5 measurements per second), (g) 1 minute averages of magnetic field vector components (R—blue line, T—green line, N—red line) and magnetic field strength (black line) as measured by FIELDS. The panels showing electron count rate also contain statistical fluctuations due to the small number of counts observed.

all eight wedges and over the bins nominally corresponding to ∼16.8–397.4 keV (bins 1–16). These are the 16 bins that were included in the first EPI-Lo public data release; although the energy of the bins has shifted in subsequent releases, the counts used in this analysis have not changed. The background, measured as the average electron count rate per one minute time bin over the period 2019 March 31–April 10 (DOY 90–100) has been subtracted from each point in the time series, and the dashed lines in these panels indicate a 2σ increase above that mean. As it is still early in the mission, a full characterization of the IS⊙IS backgrounds is ongoing and will be the subject of a later paper. The background is expected to include galactic cosmic rays and ambient heliospheric particles, including ∼2–200 keV superhalo electrons (Lin 1998; Wang et al. 2015), as well as instrumental background, such as cross-talk and electronic noise. Ultraviolet solar photons also contribute to the background of EPI-Lo (see Hill et al. 2020 for full description). To attempt to reduce random statistical fluctuations and make larger trends in the data more apparent, a second-degree Savitzky–Golay smoothing filter over 7 minutes was applied to the background-subtracted data. Further details of this smoothing technique are included in Appendix B.

The raw (i.e., unsmoothed and not background-subtracted) 1 minute electron count rate data for both telescopes are fit well by a Poisson distribution, indicating that, apart from points that lie outside the distribution, high individual peaks may not be statistically significant. The signal-to-background ratio (SBR) was examined for a variety of summing time windows in an attempt to identify periods in which multiple minutes of electron signal enhancement are clustered together. Often, solar energetic electron events are identified by the presence of energy dispersion (e.g., Krucker et al. 1999; Wang et al. 2012); however, the count statistics of the events in this study are too low to be identified in this way. We anticipate that the typical intrinsic cadence of 10 s and 1 minute of EPI-Hi and EPI-Lo, respectively, during encounters will enable precise energy dispersion analysis for larger events in the future. Using 7 minute sums of the raw 1 minute electron counts, four particular events occurring on 2019 April 2 (DOY 92) stand out with a significance of >3.5 SBR when looking at the composite significance of both instruments as defined by Equation (A1) in

Appendix A. These events are identified by arrows above Figure 2. A randomization study demonstrated a very low probability of observing this number of minutes with a composite SBR $>$ 3.5 all within the same day during a 10 day encounter period. Further details of the SBR and the randomization study may be found in Appendix A. These factors suggest that the events in question are unlikely to be random background detections. Furthermore, there were no similar intervals with a composite SBR $>$ 3.5 during Encounter 1 (2019 November 1–11) with an 8 minute time window.[17] Electron signals from individual apertures of EPI-Hi and EPI-Lo were examined, but the low statistics of the events highlighted in Figure 2 make it challenging to determine whether there is significant anisotropy.

Panels (c) and (d) in Figure 2 show the high-frequency (1.3–19.2 MHz) and low-frequency (10.5 kHz–1.7 MHz) radio data, respectively, as measured by the FIELDS V1 and V2 electric field antennas (Pulupa et al. 2017, 2020). Throughout Encounter 2, FIELDS observed solar radio emissions, including type III radio bursts and local electrostatic plasma waves (e.g., Langmuir waves). The radio bursts are primarily visible in the high-frequency radio data in the third panel, but some clearly drift down to the local electron plasma frequency in the low-frequency radio panel. The local electron plasma frequency line is visible in panel (d) of Figure 2 as a light blue line near 2×10^5 Hz. This line results from the thermal motion of the local ambient plasma near the spacecraft (Meyer-Vernet & Perche 1989). Midway through 2019 April 3 (DOY 93), the plasma frequency line drops significantly in frequency until midway through 2019 April 6 (DOY 96). Located near the plasma frequency line are small bursts of Langmuir waves. These, as well as the type III radio bursts described above, may be hard to distinguish in Figure 2 because these emissions are often highly intermittent, and there is a large amount of time covered in this plot. These emissions are more apparent in later figures that focus on narrower time periods. While Langmuir waves are often associated with solar events, Bale et al. (2019) describes a population of Langmuir waves in the inner heliosphere that do not appear to be related to solar activity. Langmuir waves may also be connected to solar wind structures, such as magnetic holes (Lin et al. 1995; MacDowall et al. 1996, 2003). Langmuir waves associated with magnetic holes may be caused by adiabatic focusing of electrons of thermal energies in the magnetic field depression.

Panels (e) and (f) in Figure 2 show the solar wind proton density and radial velocity moments, respectively, as measured by the SWEAP Solar Probe Cup (Case et al. 2020). Examining the solar wind moments together with the magnetic field, it is clear that the characteristics of the spacecraft's local plasma environment change significantly throughout this time period, which includes periods of dense solar wind (and associated changes in the plasma line in panel (d) of Figure 2) throughout the beginning of the encounter that resume after perihelion on 2019 April 6 (DOY 96) due to Parker Solar Probe's magnetic connection to streamer flows (Rouillard et al. 2020). There is a lack of consistent timing between these density structures and the observed enhancements in electrons.

[17] The EPI-Lo electron integration time during Encounter 1 was 4 minutes, making it impossible to examine the same 7 minute window investigated during Encounter 2. When using an 8 minute time window for Encounter 2, the four events identified on 2019 April 2 are still the only cases with SBR $>$ 3.5.

Panel (g) of Figure 2 shows the radial–tangential–normal (RTN) vector components of the magnetic field measured by FIELDS during Parker Solar Probe's second encounter. A line pointing from the center of the Sun to the spacecraft defines the radial axis (radial component shown as a blue line). The cross product of the Sun's rotational axis vector with the radial axis determines the tangential axis (tangential component shown as a green line). The normal axis completes the right-handed orthonormal basis (red line). The black line in this panel shows the magnitude of the magnetic field vector as a function of time. Over the course of Encounter 2, the magnetic field was generally directed toward the Sun (see the predominant large negative R component). In addition, there are many rotations in the magnetic field vector in which components of the magnetic field vector rapidly change polarity, a subset of which are referred to as switchbacks (Bale et al. 2019), along with a number of depressions in the magnetic field strength.

As will be discussed further in the following section, most of the IS⊙IS electron events (three of four) during Encounter 2 show temporal correspondence between the two telescopes, and all four show temporal correspondence with contextual data, including radio bursts, Langmuir waves, and magnetic field rotations and depressions detected by FIELDS. Events that exhibit temporal correspondence between the two IS⊙IS instruments are unlikely to be due to the detection of different species of charged particles (i.e., electrons and ions) from the same source because of the substantially different travel times of energetic ions and electrons.

5. 2019 April 2 Electron Events

Figure 3 highlights (in the same format as Figure 2, with the addition of the azimuthal magnetic field angle in panel (h)) the full day of 2019 April 2 (DOY 92) when the largest increases in electron count rate observed by both instruments (indicated by arrows above Figure 3 at ∼03:00, 05:00, 09:00, and 15:40 UTC), as well as several strong type III radio bursts, occurred. Figure 3 shows that in some cases an electron enhancement was observed in one instrument but not the other. However, this is not uncommon: IS⊙IS has detected a number of proton events in which enhancements are primarily seen in one of the instruments, including a CME-associated enhancement detected by EPI-Lo during Encounter 1 (McComas et al. 2019; Giacalone et al. 2020; Hill et al. 2020; Mitchell et al. 2020) and an SEP event primarily detected by EPI-Hi on 2019 April 4 (DOY 94) (McComas et al. 2019; Leske et al. 2020).

We feature the electron events on 2019 April 2 (DOY 92) at ∼03:00, 05:00, 09:00, and 15:40 UTC in the following sections as examples of IS⊙IS electron measurements that are unlikely to be due to background.

5.1. EPI-Hi Event on DOY 92 at ∼03:00 UTC

Panel (a) of Figure 4 shows a prolonged increase in the electron count rate measured by EPI-Hi beginning at ∼02:50 UTC and returning to background levels at ∼03:28 UTC. EPI-Lo did not observe an electron enhancement during this EPI-Hi event, but as mentioned previously, there are several examples of events seen primarily in just one of these instruments. The first 4 hr of 2019 April 2 (DOY 92), when Parker Solar Probe was at a heliocentric distance of just over 0.19 au, were also characterized by several dramatic rotations in the magnetic field vector coupled to substantial dips in the magnetic field strength

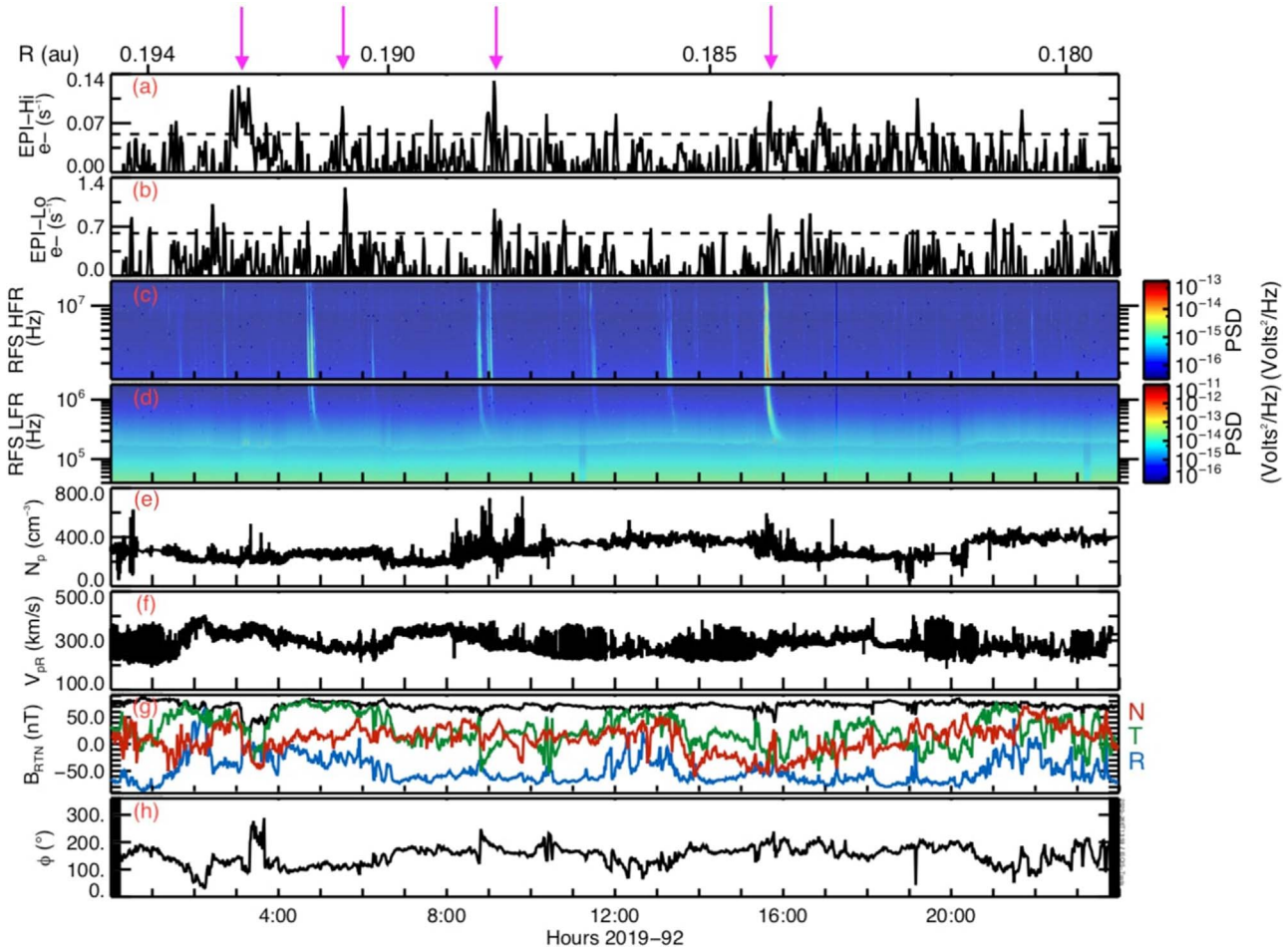

Figure 3. Overview of 2019 April 2 (DOY 92) following the format of Figure 2 but with the addition of the azimuthal magnetic field angle (in RTN coordinates) in panel (h). Electron events of particular interest during this day occur at approximately 03:00, 05:00, 09:00, and 15:40 UTC in the top two panels. Arrows at the top of the figure indicate events that will be highlighted in this work.

as shown in panels (g)–(i) of Figure 4. Between ∼02:15 and ∼02:30 UTC, the radial field (blue line in panel (h)) transitions from strongly positive to strongly negative with a temporary decrease in the field intensity (marked by the blue arrow in Figure 4), suggesting the crossing of a heliospheric current sheet (Szabo et al. 2020). Just after 03:00 UTC, the magnitude of the local magnetic field (panel (g)) dipped from the range of 70–75 nT, characteristic throughout this day, down to <10 nT (marked by the orange arrow in Figure 4). This occurred in conjunction with a polarity reversal in the normal component of the magnetic field from strongly positive to strongly negative. This particular dip lasts until ∼03:25 UTC, at which point it recovers to ∼50 nT. The EPI-Hi electron enhancement overlaps in time with this magnetic field dip and is preceded by the reversal of the radial component of the magnetic field. At ∼03:38 UTC, the magnetic field strength dips again to <5 nT. The magnetic field strength returns to its approximate ambient state near 04:00 UTC (marked by the magenta arrow in Figure 4). During each of the dips in field strength, groups of Langmuir waves are observed near the local plasma frequency in the low-frequency radio data (indicated with red arrows in panel (d) of Figure 4). The timing between these changes in the magnetic field and the EPI-Hi electron enhancement suggests that the electron increase may be linked to this rotation and depression in the magnetic field. It is interesting to observe this electron enhancement in the vicinity of a current sheet; however, the low Alfvén speed (∼100 km s^{-1}) in the region around this event makes it unlikely that these electrons were accelerated by reconnection in the local environment of the spacecraft (Phan et al. 2013).

The FIELDS instrument observed a type III radio burst just before the electron enhancement, starting at 02:42 UTC (Figure 4), which raises the possibility that the electrons observed in situ might have been related to the electrons that generated the radio emissions. That said, this radio burst was not clearly observed to drift to the local electron plasma line, and thus, according to the interpretation of Cane & Erickson (2003), the electron beam from that particular radio burst likely missed the spacecraft. Thus, we believe that this electron event is unlikely to be connected to that radio burst. Figure 4 shows other type III radio bursts that do not appear to be associated with significant increases in the electron intensity.

5.2. EPI-Hi and EPI-Lo Events on DOY 92 at ∼05:00 and ∼09:00 UTC

Figure 5 shows the time period between 04:30 and 10:00 UTC on 2019 April 2 (DOY 92). A small increase in the electron signal, observed at ∼05:30 UTC, is nearly concurrent in both EPI-Hi and EPI-Lo. During the period shown in

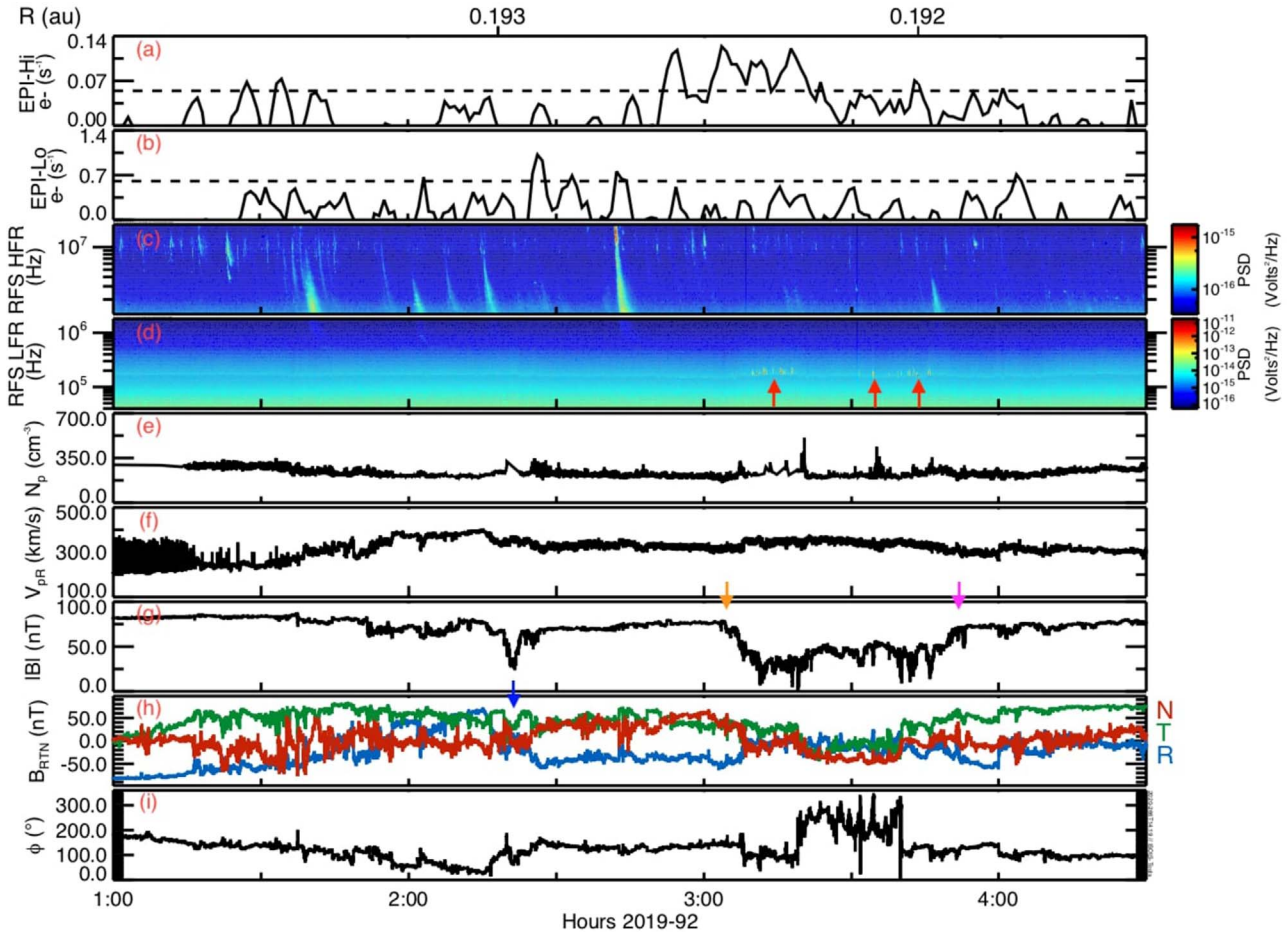

Figure 4. Overview of 01:00–04:30 UTC on 2019 April 2 (DOY 92). A prolonged increase in the EPI-Hi electron count rate is shown in panel (a), beginning at 02:50 UTC. No obvious accompanying increase in the EPI-Lo electron count rate is observed in panel (b). Panel (g) shows several depressions in the magnetic field strength coupled to significant rotations in the magnetic field vector shown in panel (h) (note that higher-cadence magnetic field data are used in this plot to accurately portray the timing of these features). The azimuthal magnetic field angle is plotted in panel (i) to show these rotations. Some of these magnetic depressions appear to have associated Langmuir waves visible in the low-frequency radio data along the local plasma frequency (indicated with red arrows in panel (d)). A number of type III radio bursts are observed throughout this time period in the high-frequency radio data (panel (c)).

Figure 5, two groups of type III radio bursts drift down to the local plasma frequency line located around 2×10^5 Hz in Figure 5. The fact that the radio signal extends down to the local plasma line suggests that the source of electrons responsible for these enhancements is well connected to the spacecraft and that the electrons responsible for the type III radio burst reached the local environment of the spacecraft according to Cane & Erickson (2003). However, it should be noted that Langmuir waves were not observed related to this event. Another type III radio burst was observed at ∼06:15 UTC but does not appear to reach the local plasma frequency line.

The electron increase just before ∼05:30 UTC may be associated with the first group of strong radio bursts visible in the high-frequency radio data that begins at ∼04:41 UTC. The delay between the onset of the type III emissions and the electron enhancement in this case (∼40 minutes) is longer than the high end of the similar delays observed by Haggerty & Roelof (2002) at 1 au (∼24 minutes). However, more Parker Solar Probe observations of electron events and type III radio bursts are required to understand their temporal relationship close to the Sun and whether this delay is reasonable.

Figure 5 shows that EPI-Hi observed a cluster of statistically significant increases in electron count rate starting at ∼08:52 UTC. EPI-Lo observed a similar cluster of increases in electron signal starting at ∼09:04 UTC. During this time period, the FIELDS electric field antennas observed two groups of type III radio bursts commencing at ∼08:42 UTC and ∼08:57 UTC on April 2 (DOY 92), with several distinct bursts over this time period (shown in panels (c) and (d) of Figure 5). The first type III radio burst clearly drifts to the local plasma frequency in panel (d), implying that the electrons reached the local environment of the spacecraft. Around 08:45 UTC, the tangential component of the magnetic field also abruptly reversed from strongly positive to strongly negative. The clusters of electron enhancement in EPI-Hi and EPI-Lo were well timed with the type III radio bursts and the rotation in the magnetic field. The delay between the onset of the type III radio bursts and the start of the electron signal in both instruments is well within the expectations from the data sets presented by Haggerty & Roelof (2002) and Cane (2003) when accounting for the differences in travel time between 1 au transport and 0.19 au transport. The statistics of these events are too low to analyze possible energy dispersion, but future events with higher statistics will allow this analysis.

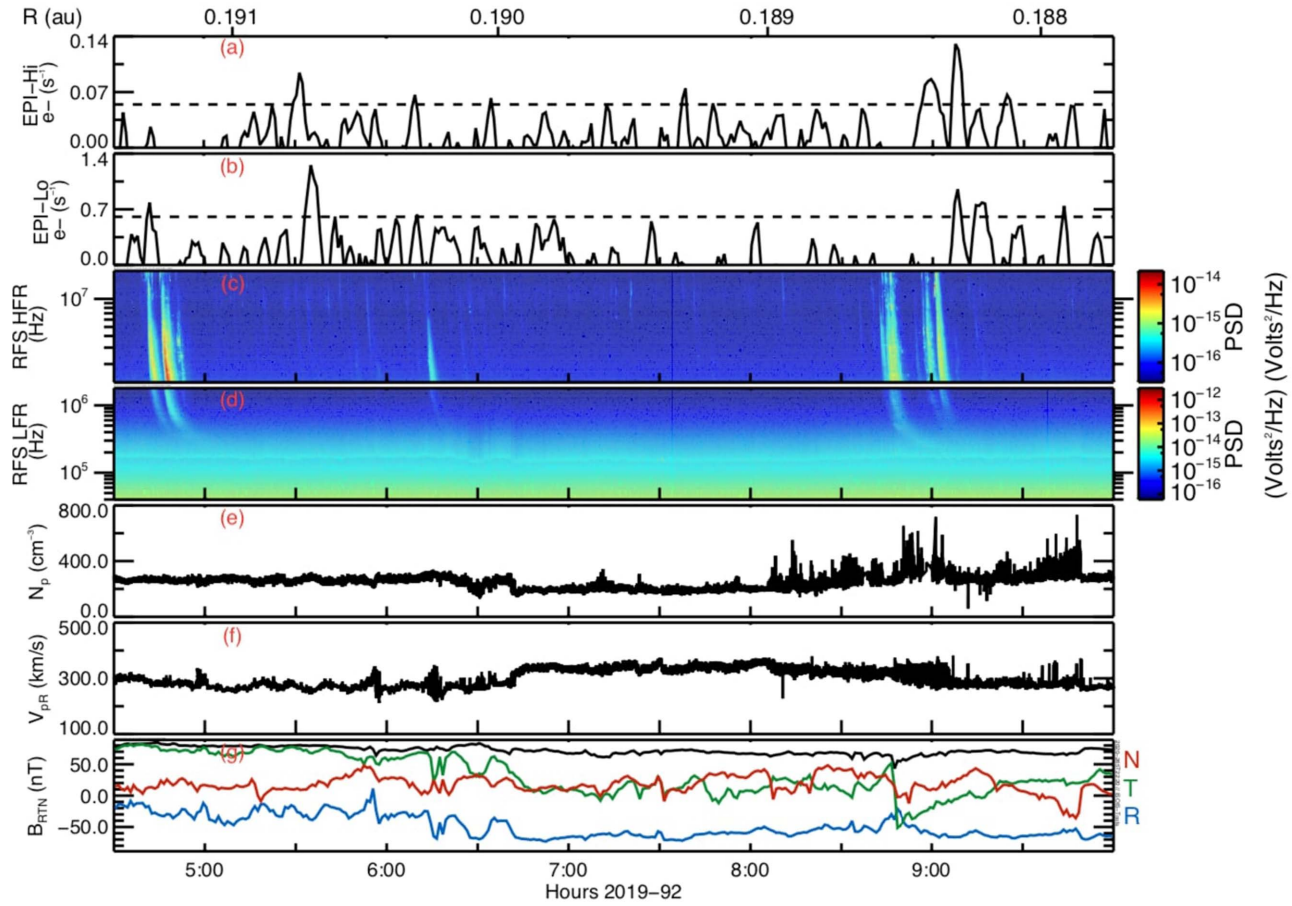

Figure 5. Overview of the time around the radio and electron events on 2019 April 2 (DOY 92) at ∼05:40 and ∼09:00 UTC. Sharp peaks in electron count rate are seen in both EPI-Hi (panel (a)) and EPI-Lo (panel (b)). Strong radio bursts are seen in the high-frequency radio data (panel (c)) drifting down to the local plasma frequency, which is visible in the low-frequency radio data (panel (d)). The tangential component of the magnetic field switches from strongly positive to strongly negative at ∼08:50 UTC in panel (g).

5.3. EPI-Hi and EPI-Lo Event on DOY 92 at ∼15:40 UTC

At ∼15:32 UTC on 2019 April 2 (DOY 92), both EPI-Hi and EPI-Lo observed a $>2\sigma$ increase in electron signal. Around the same time, the FIELDS electric field probes detected a type III radio burst (Figure 6). By 16:00 UTC, the radio signal drifted down to the plasma frequency line, concurrent with the appearance of several groups of Langmuir waves. These features indicate that the associated electron beam likely reached the local environment of the spacecraft. This radio burst also exhibits slowly drifting, type II-like features that appear to be striae caused by nonuniformities in the source plasma environment as discussed in Pulupa et al. (2020). A small dip in the magnetic field strength occurs nearly concurrently with the Langmuir waves and the radio burst meeting the local plasma frequency. The peak of the electron increase occurs at ∼15:40 UTC, 8 minutes after the arrival of the ∼8 MHz radio signal at Parker Solar Probe. The electron event is still present but reduced in amplitude when the radio signal reaches the local plasma frequency line. This may be an example of an event without a delayed energetic electron signal as reported within the data sets of Krucker et al. (1999) and Haggerty & Roelof (2002). Over the next hour, EPI-Hi observed a series of temporally extended electron enhancements, with durations of ∼30 minutes, uncharacteristic of the EPI-Hi electron signal throughout Encounter 2. However, they do not reach the required SBR level to be considered in this study.

In addition to the electron enhancements on this day, EPI-Lo observed a significant ion event beginning at ∼10:30 UTC on 2019 April 2 (DOY 92) and lasting until ∼07:00 UTC on 2019 April 3 (DOY 93) (Leske et al. 2020). This event had signatures of an impulsive SEP event, including energy dispersion, an enrichment in heavy ions, a small increase in ^{3}He, and strong anisotropies (E. C. Roelof 2020, personal communication). The low electron statistics preclude any conclusive comparison with the ion observations.

5.4. Radio Bursts Extending to the Local Plasma Frequency

FIELDS observed hundreds of type III radio bursts during Encounter 2, but only three radio bursts were clearly observed to extend to the local plasma frequency. These three events were featured in earlier sections, occurring at ∼05:00, 09:00, and 15:40 UTC on 2019 April 2 (DOY 92) (Figure 3) and were associated with significant electron increases observed by EPI-Hi and EPI-Lo. Another pair of radio bursts, starting at ∼16:55 UTC on 2019 April 5 (DOY 95), extended very nearly to the local plasma frequency line, prompting the question of whether these bursts are also associated with evidence of an electron enhancement. Figure 7 shows the time period around the radio burst on 2019 April 5 (DOY 95) at 16:55 UTC. During this

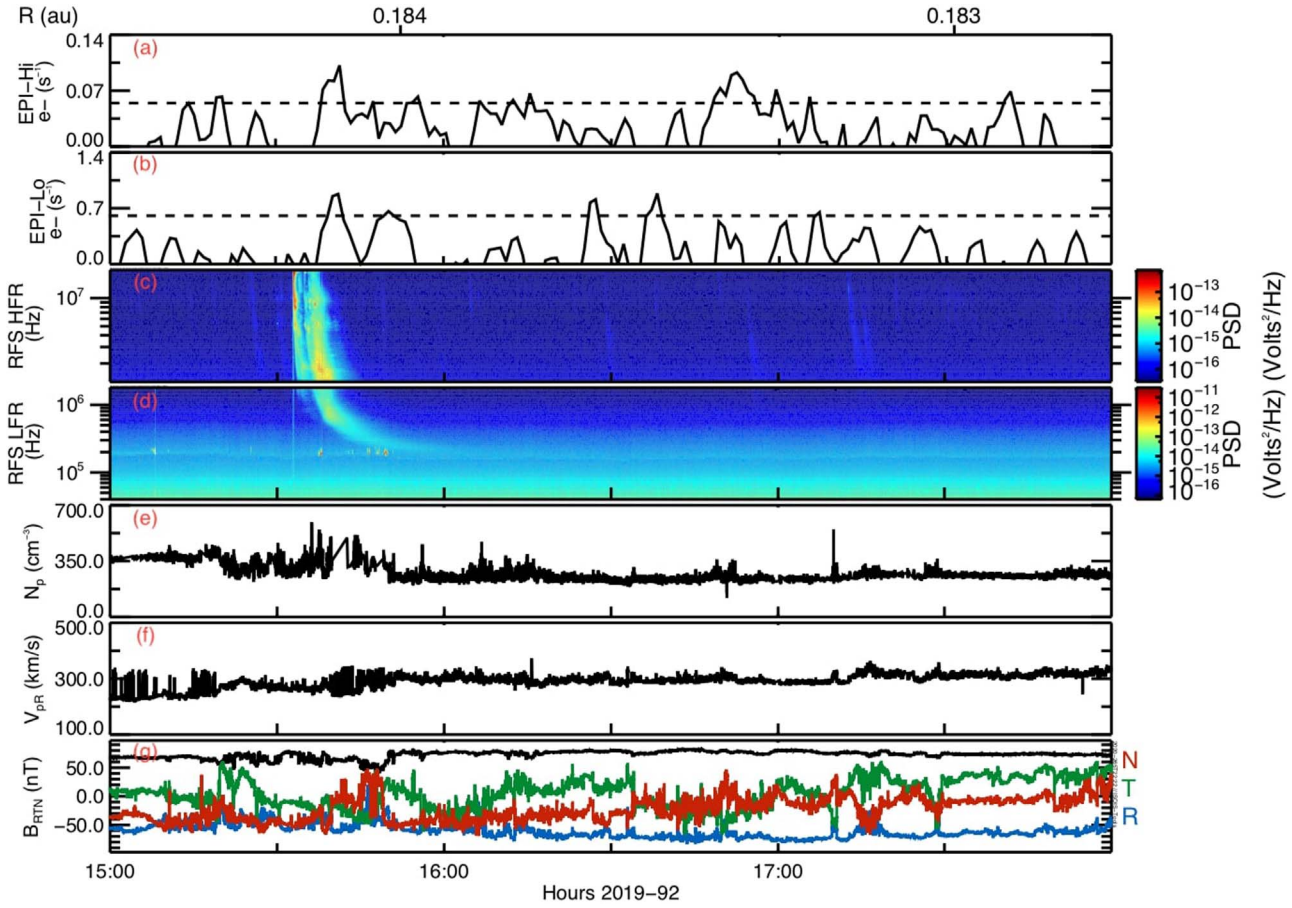

Figure 6. Overview of the time around the radio and electron event on 2019 April 2 (DOY 92) at 15:40 UTC. Increases in both EPI-Hi (panel (a)) and EPI-Lo (panel (b)) are observed that appear to be connected to the preceding radio burst visible in the high-frequency radio data starting at 15:32 UTC (panel (c)), drifting down to the local plasma frequency line in the low-frequency radio data (panel (d)). Nearly concurrent with the radio burst drifting to the local plasma frequency, a number of Langmuir waves are visible. A number of small depressions are visible in the magnetic field strength, most notably at ∼15:47 UTC (panel (g)—note the use of higher-cadence magnetic field data).

time, Parker Solar Probe is in the region of lower density discussed in Section 4 (see also Figure 2), such that the plasma line is located at a lower frequency, making it more challenging to resolve in Figure 7. In this figure, the plasma frequency line can be inferred from the location of several Langmuir waves observed throughout the time period and the magenta arrow in panel (d). The EPI-Hi and EPI-Lo electron signals show a small concurrent enhancement above 2σ after the first radio burst (panels (a) and (b) of Figure 7). This electron enhancement is not as large as those featured in earlier sections but is nearly concurrent between the two instruments and peaks less than 10 minutes after the start of the type III radio burst, suggesting that it may be associated with the type III bursts. There are several other radio bursts during Encounter 2 that appear to come close to reaching the plasma frequency line but do not clearly reach it. There is not a one-to-one correlation between the radio bursts that approach, but do not clearly reach, the plasma line and electron enhancements in both instruments. However, both measurements are at the threshold of observability because they are so small compared to the background.

The association between radio bursts that extend to the local plasma frequency and a corresponding enhancement in the electron signals in both EPI-Hi and EPI-Lo suggests that the IS⊙IS telescopes are observing solar electron events. This correlation is also consistent with the arguments made by Cane & Erickson (2003) that the radio signal reaching the local plasma frequency indicates that the electron beam has reached the local environment of the spacecraft.

6. Summary and Discussion

In this study, we presented the first observations of energetic electron events within 0.2 au of the Sun during Parker Solar Probe's second encounter. The Helios missions at 0.3–1 au from the Sun demonstrated that there are many electron events observable close to the Sun that may not be observable at 1 au. Since Parker Solar Probe has a significantly shorter perihelion distance than Helios, we would expect to see even smaller events than Helios observed. The early Parker Solar Probe encounters occurred during solar minimum conditions, and no significant energetic electron events were observed during Encounter 1. During Encounter 2, the IS⊙IS instrument suite observed four electron enhancements with SBR $>$ 3.5. The detection of electron enhancements appears consistent with the clear increase in the occurrence of type III radio bursts observed during Encounter 2, although there are many more type III radio bursts than electron events. Factors, such as concurrent or nearly concurrent electron enhancements seen by both instruments, abrupt changes in the magnetic field vector or strength, plausibly associated type III radio bursts that reach the

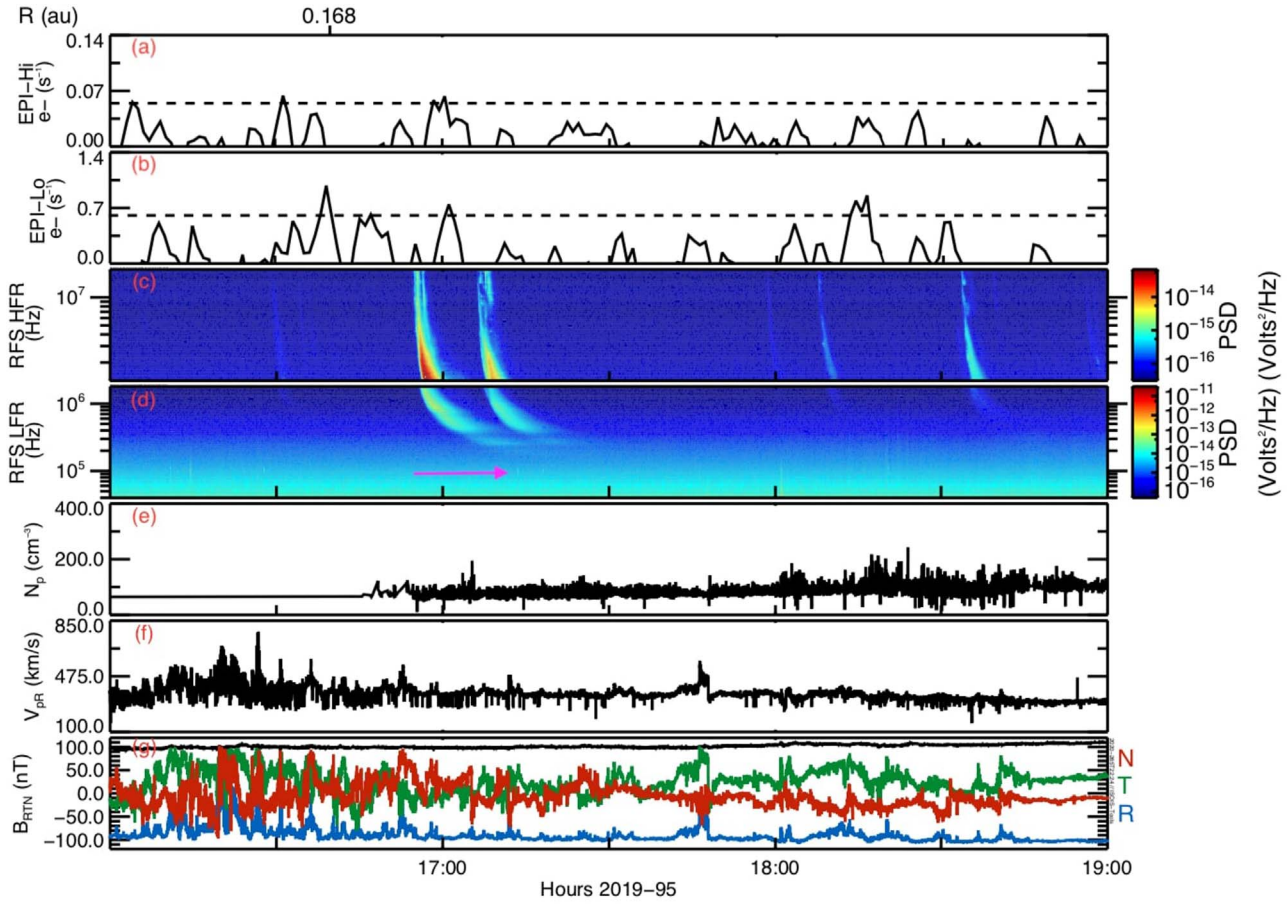

Figure 7. Overview of the time around the radio and electron event on 2019 April 5 (DOY 95) at 17:00 UTC. A strong radio burst is visible in the high-frequency radio data starting at 16:55 UTC (panel (c)), which drifts down to the local plasma frequency line in the low-frequency radio data (marked by the magenta arrow in panel (d)). Marginal increases in both EPI-Hi (panel (a)) and EPI-Lo (panel (b)) at ~17:00 UTC are observed that may be connected to this radio burst.

local plasma frequency, and the presence of Langmuir waves, suggest that the events highlighted in this work are indeed energetic electron events and not simply random fluctuations in the instrumental background. We therefore conclude that these are the first measurements of energetic electrons within 0.2 au.

These first measurements suggest that, as Parker Solar Probe continues to approach the Sun and solar cycle 25 starts to develop, Parker Solar Probe is likely to provide further insight into the characteristics of energetic electron events in the inner heliosphere. While the statistics of these energetic electron events are too low for us to draw firm physical conclusions, they suggest the presence of smaller solar electron events than previously reported. The acceleration mechanisms at the Sun that produce such small and short-duration energetic electron enhancements require further investigation. In addition, the event at 03:00 UTC on 2019 April 2 appeared associated with changes in the interplanetary magnetic field, suggesting that local acceleration may have occurred. However, the low Alfvén speed suggests that conditions were not favorable for acceleration by reconnection. Other issues raised by these observations include why there may be a variable delay between the type III radio emissions and the energetic electron enhancements, which might arise from a delayed injection or transport effects, and why some events were seen only in EPI-Hi and not EPI-Lo. Factors such as energy dispersion and anisotropy will help identify future IS⊙IS energetic electron events and provide valuable insight into their sources and the timing of high- and low-energy electrons. We anticipate that such questions about the nature of small electron events will be answered by observations from future Parker Solar Probe encounters.

We wish to acknowledge the support of NASA's Parker Solar Probe grant NNN06AA01C. We thank the Parker Solar Probe IS⊙IS, FIELDS, and SWEAP teams, including the engineers, technicians, administrators, and scientists, who developed the instruments used in this study. The IS⊙IS data and visualization tools are available to the community at: https://spacephysics.princeton.edu/missions-instruments/isois; data are also available via the NASA Space Physics Data Facility (https://spdf.gsfc.nasa.gov/).

Appendix A
Calculations of Signal-to-background Ratio

The composite SBR of both EPI-Lo and EPI-Hi is calculated as

$$\mathrm{SBR}_{\mathrm{comp}} = \frac{\left[\left(\sum_1^j N_{\mathrm{hi}}\right) - jB_{\mathrm{hi}}\right] + \left[\left(\sum_1^j N_{\mathrm{lo}}\right) - jB_{\mathrm{lo}}\right]}{\sqrt{\left(\sum_1^j N_{\mathrm{hi}}\right) + \left(\sum_1^j N_{\mathrm{lo}}\right)}} \quad \text{(A1)}$$

where j is the number of minutes in the summing time window, $N_{\mathrm{hi/lo}}$ is the raw count data for each 1 minute time bin in EPI-Hi and EPI-Lo respectively, and $B_{\mathrm{hi/lo}}$ is the background in EPI-Hi (7.6 counts) and EPI-Lo (14.4 counts) respectively, defined as the average number of counts per 1 minute time bin throughout Encounter 2. For example, the maximum number of counts per 1 minute time bin during the ∼05:00 UTC event was 16 counts in EPI-Hi and 25 counts in EPI-Lo. Three of the four events with >3.5 composite SBR also have SBR > 2.5 separately in both individual instruments.

The composite SBR data show seven individual 1 minute time bins with SBR > 3.5, all occurring on 2019 April 2 (DOY 92). Randomizing the raw 1 minute electron count bins throughout Encounter 2 and performing the same SBR analysis with a 7 minutes window resulted in a 0.2% probability that a random trial could produce seven individual 1 minute time bins with SBR > 3.5 throughout an encounter. This likelihood is further reduced by the fact that the random trials do not produce these events on the same day. There is a 1×10^{-6} chance of all seven individual 1 minute time bins with SBR > 3.5 occurring on the same day over a time period of 10 days by random coincidence. Since we are examining a period of 10 days, this is calculated as $P = (1/10)^6$, assuming that the first event sets the day and the other six must then randomly occur on that day.

Appendix B
Signal Filtering

A Savitzky–Golay filter fits a polynomial of a certain degree as a weighted moving average to the time series (Savitzky & Golay 1964). A Savitzky–Golay filter may be used to smooth data while preserving important features that would be lost using a boxcar average (e.g., Williams & Pesnell 2011). To investigate both smoothing techniques, the distribution of the widths of the electron events was compared when using a Savitzky–Golay filter and when using a boxcar average. It was found that the boxcar average significantly increased the width and mean of the distribution compared with the Savitzky–Golay filter, resulting in electron events that appear artificially wider. A second-degree Savitzky–Golay filter applied over 7 minutes succeeded in reducing random statistical fluctuations and making significant electron enhancements more obvious.

ORCID iDs

J. G. Mitchell https://orcid.org/0000-0003-4501-5452
G. A. de Nolfo https://orcid.org/0000-0002-3677-074X
M. E. Hill https://orcid.org/0000-0002-5674-4936
E. R. Christian https://orcid.org/0000-0003-2134-3937
D. J. McComas https://orcid.org/0000-0001-6160-1158
N. A. Schwadron https://orcid.org/0000-0002-3737-9283
S. D. Bale https://orcid.org/0000-0002-1989-3596
A. W. Case https://orcid.org/0000-0002-3520-4041
C. M. S. Cohen https://orcid.org/0000-0002-0978-8127
C. J. Joyce https://orcid.org/0000-0002-3841-5020
J. C. Kasper https://orcid.org/0000-0002-7077-930X
A. W. Labrador https://orcid.org/0000-0001-9178-5349
R. A. Leske https://orcid.org/0000-0002-0156-2414
R. J. MacDowall https://orcid.org/0000-0003-3112-4201
D. G. Mitchell https://orcid.org/0000-0003-1960-2119
M. Pulupa https://orcid.org/0000-0002-1573-7457
I. G. Richardson https://orcid.org/0000-0002-3855-3634
M. L. Stevens https://orcid.org/0000-0002-7728-0085
J. R. Szalay https://orcid.org/0000-0003-2685-9801

References

Anderson, K., & Lin, R. 1966, PhRvL, 16, 1121
Arnoldy, R., Hoffman, R., & Winckler, J. 1960, JGR, 65, 3004
Bale, S., Badman, S., Bonnell, J., et al. 2019, Natur, 576, 237
Bale, S. D., Goetz, K., Harvey, P. R., et al. 2016, SSRv, 204, 49
Bastian, T., Benz, A., & Gary, D. 1998, ARA&A, 36, 131
Bialk, M., & Dröge, W. 1993, ICRC (Calgary), 3, 278
Bieber, J., Earl, J., Green, G., et al. 1980, JGR, 85, 2313
Buttighoffer, A. 1998, A&A, 335, 295
Cane, H. 2003, ApJ, 598, 1403
Cane, H., & Erickson, W. 2003, JGRA, 108, 1203
Case, A. W., Kasper, J. C., Stevens, M. L., et al. 2020, ApJS, 246, 43
Crooker, N., Gosling, J., & Kahler, S. 2002, JGRA, 107, 1028
Crooker, N., & Webb, D. 2006, JGRA, 111, 8108
Drake, J. F., Cassak, P. A., Shay, M. A., Swisdak, M., & Quataert, E. 2009, ApJL, 700, L16
Drake, J. F., & Swisdak, M. 2012, SSRv, 172, 227
Drake, J. F., Swisdak, M., Che, H., & Shay, M. A. 2006, Natur, 443, 553
Dresing, N., Effenberger, F., Gómez-Herrero, R., et al. 2020, ApJ, 889, 143
Dröge, W. 2000, ApJ, 537, 1073
Dulk, G. A., Leblanc, Y., Robinson, P. A., Bougeret, J.-L., & Lin, R. P. 1998, JGR, 103, 17223
Ergun, R., Larson, D., Lin, R., et al. 1998, ApJ, 503, 435
Fox, N. J., Velli, M. C., Bale, S. D., et al. 2016, SSRv, 204, 7
Frank, L. 1965, JGR, 70, 1593
Giacalone, J., Mitchell, D., Allen, R., et al. 2020, ApJS, 246, 29
Haggerty, D. K., & Roelof, E. C. 2002, ApJ, 579, 841
Halekas, J., Whittlesey, P., Larson, D., et al. 2020, ApJS, 246, 22
Hill, M., Mitchell, D., Allen, R., et al. 2020, ApJS, 246, 65
Hill, M., Mitchell, D., Andrews, G., et al. 2017, JGRA, 122, 1513
Hoffman, R. A., Davis, L. R., & Williamson, J. M. 1962, JGR, 67, 5001
Hsieh, K., & Simpson, J. 1970, ApJL, 162, L191
Hurford, G., Mewaldt, R., Stone, E., & Vogt, R. 1975, ApJL, 201, L95
Kasper, J. C., Abiad, R., Austin, G., et al. 2016, SSRv, 204, 131
Klassen, A., Bothmer, V., Mann, G., et al. 2002, A&A, 385, 1078
Krucker, S., Kontar, E., Christe, S., Glesener, L., & Lin, R. 2011, ApJ, 742, 82
Krucker, S., Larson, D. E., Lin, R. P., & Thompson, B. J. 1999, ApJ, 519, 864
Leske, R., Christian, E., Cohen, C., et al. 2020, ApJS, 246, 35
Lin, N., Kellogg, P., MacDowall, R., et al. 1995, GeoRL, 22, 3417
Lin, R. 1970, SoPh, 12, 266
Lin, R. 1974, SSRv, 16, 189
Lin, R. 1985, SoPh, 100, 537
Lin, R. 1998, The Advanced Composition Explorer Mission (Berlin: Springer), 61
Lin, R., Larson, D., Ergun, R., et al. 1997, AdSpR, 20, 645
Lin, R., Levedahl, W., Lotko, W., Gurnett, D., & Scarf, F. 1986, ApJ, 308, 954
Lin, R., Potter, D., Gurnett, D., & Scarf, F. 1981, ApJ, 251, 364
MacDowall, R., Lin, N., & McComas, D. 2003, AdSpR, 32, 479
MacDowall, R. J., Lin, N., Kellogg, P. J., et al. 1996, in AIP Conf. Proc. 382, Langmuir Waves in Magnetic Holes: Source Mechanism and Consequences, ed. D. Winterhalter et al. (Melville, NY: AIP), 301
McComas, D., Christian, E., Cohen, C., et al. 2019, Natur, 576, 223
McComas, D. J., Alexander, N., Angold, N., et al. 2016, SSRv, 204, 187
Meyer-Vernet, N., & Perche, C. 1989, JGR, 94, 2405
Mitchell, D. G., Giacalone, J., Allen, R. C., et al. 2020, ApJS, 246, 59
Phan, T., Shay, M., Gosling, J., et al. 2013, GeoRL, 40, 4475
Pulupa, M., Bale, S., Bonnell, J., et al. 2017, JGRA, 122, 2836
Pulupa, M., Bale, S. D., Badman, S. T., et al. 2020, ApJS, 246, 49
Reames, D. V. 2002, ApJL, 571, L63
Reames, D. V. 2013, SSRv, 175, 53
Reames, D. V., & Ng, C. K. 2004, ApJ, 610, 510
Reid, H. A. S., & Ratcliffe, H. 2014, RAA, 14, 773
Rouillard, A. P., Kouloumvakos, A., Vourlidas, A., et al. 2020, ApJS, 246, 37
Savitzky, A., & Golay, M. J. 1964, AnaCh, 36, 1627
Szabo, A., Larson, D., Whittlesey, P., et al. 2020, ApJS, 246, 47
Tan, L. C., Reames, D. V., Ng, C. K., Shao, X., & Wang, L. 2011, ApJ, 728, 133

Thompson, W. 2006, A&A, 449, 791
Van Allen, J. A., & Krimigis, S. 1965, JGR, 70, 5737
Vourlidas, A., Howard, R. A., Plunkett, S. P., et al. 2016, SSRv, 204, 83
Wang, L., Krucker, S., Mason, G. M., Lin, R. P., & Li, G. 2016, A&A, 585, A119
Wang, L., Lin, R., & Krucker, S. 2011, ApJ, 727, 121
Wang, L., Lin, R., Krucker, S., & Mason, G. M. 2012, ApJ, 759, 69
Wang, L., Lin, R. P., Krucker, S., & Gosling, J. T. 2006, GeoRL, 33, L03106
Wang, L., Yang, L., He, J., et al. 2015, ApJL, 803, L2
Whittlesey, P. L., Larson, D. E., Kasper, J. C., et al. 2020, ApJS, 246, 74
Wibberenz, G., & Cane, H. 2006, ApJ, 650, 1199
Wiedenbeck, M. E., Angold, N. G., Birdwell, B., et al. 2017, ICRC (Busan), 35, 16
Williams, P. E., & Pesnell, W. D. 2011, JPhCS, 271, 012082